The Electrochemical Society
Advancing solid state & electrochemical science & technology

Corrosion of Binder Jetting Additively Manufactured 316L Stainless Steel of Different Surface Finish

Corrosion of Binder Jetting Additively Manufactured 316L Stainless Steel of Different Surface Finish

Masoud Atapour,[1,2,z] Xuying Wang,[1] Mats Persson,[3] Inger Odnevall Wallinder,[1] and Yolanda S. Hedberg[1,z,*]

[1]KTH Royal Institute of Technology, Dept. Chemistry, Div. Surface and Corrosion Science, SE-10044, Stockholm, Sweden
[2]Department of Materials Engineering, Isfahan University of Technology, Isfahan, 84156-83111, Iran
[3]Digital Metal AB, c/o Höganäs AB, S-26383 Höganäs, Sweden

One technique of additive manufacturing is the binder-jetting technique that has the advantages of low costs, printing at room temperature and in air, and no need of a support structure. The aim of this study was to investigate the corrosion behavior of printed 316L surfaces with and without different post surface treatments of blasting and superfinishing. Comparative studies were performed on abraded wrought 316L. Surface topography, porosity, surface oxide composition, and electrochemical characteristics, including pitting corrosion, were investigated at room temperature as a function of post surface treatments in diluted hydrochloric acid at pH 1.5. The blasting and superfinishing treatment significantly reduced the surface roughness and level of surface porosity. Blasting detrimentally affected on the pitting corrosion resistance. The superfinishing process induced an enrichment of chromium in the surface oxide and improved the pitting corrosion resistance. All surfaces revealed slightly reduced susceptibility to pit initiation and metastable pitting as compared to wrought 316L, possibly explained by the absence of inclusions. Once pitting propagation was induced, repassivation was hindered for all surfaces compared with the wrought surface. The pitting corrosion resistance of the as-superfinished 316L was improved compared with wrought 316L.

The additive manufacturing (AM) technology is currently exhibiting the fastest growth in manufacturing enterprises and is considered one of the key components of the 4th industrial revolution.[1] This technology is characterized by substantially higher dimensional accuracy, material flexibility, design freedom, and lower cost, compared to conventional manufacturing techniques. AM technology, which is based on an incremental layer-by-layer process using computer-aided design, facilitates the fabrication of complex or customized parts in an inexpensive process.[2] This technique has been widely applied to fabricate high performance components for e.g. aerospace, medicine, and energy and automotive applications.[2] Advantages and disadvantages for different material groups and applications using several AM technologies have been recently reviewed in Refs. 2–4. There is a growing interest in developing AM technologies for the fabrication of different metallic materials.[5] Selective laser melting (SLM), an AM technique based on powder bed fusion, has been widely utilized for metals. The SLM method to produce metallic components is today often superior in terms of corrosion properties as compared to traditional manufacturing methods, such as casting or rolling.[6,7] Nevertheless, it also has specific drawbacks such as the formation of non-equilibrium microstructures, the availability of a limited number of metal/alloy powders, a necessary support structure, the formation of molten pool boundaries, and a high level of residual stresses.[8–10] An alternative AM method is the binder jetting (BJ) AM technology, in which the parts are built layer-by-layer by applying a binder between each metal powder layer prior to sintering. BJ was invented in 1993 at the Massachusetts Institute of Technology, US, and has been developed by several companies in the world.[11–13] It has been concluded that the improvement of the post processing has one of the greatest potentials for advancing the BJ technology. However, porosity and limited mechanical properties are considered the main challenges of the BJ technique.[14,15] The printing procedure is carried out at room temperature without any protective atmosphere.[16] The printed components are finally sintered at optimal temperature and may

also receive post-processing such as blasting and surface finish. High productivity, good surface quality and low costs have been claimed the main advantages of the BJ 3D printing technology,[17] along with the absence of distortion and residual stresses since the process is conducted at room temperature. The process is able to produce complex AISI 316L stainless steel parts with a density up to 97% without any dependence on the printing orientation.[18] However, many aspects of the performance, including the corrosion behavior, of these printed products of 316L are still unknown.[12] 316L is an austenitic stainless steel of low carbon content (⩽0.03 wt%) and high corrosion resistance but shows, depending on exposure conditions, a susceptibility to local corrosion phenomena.

It has been reported that the surface roughness of metallic products fabricated by traditional AM methods, such as SLM, can be as high as 10–30 μm,[19,20] while the typical roughness of the BJ printed and as-sintered surfaces is approximately 6 μm. Different post surface treatments can for both products be applied to reduce the roughness. The surface roughness and material interactions induced by different surface finishing processes influence the corrosion resistance.[21–23] It has for example been reported that sand blasting and brushing can improve the resistance to pitting corrosion and stress corrosion cracking of 316L in 3.5% NaCl,[21] and improved corrosion resistance has also been reported for 316L in 1 M NaCl after a combined sand blasting and surface finishing.[24] Beneficial effects of mechanical laser shock processing, but detrimental effects of thermo-mechanical laser shock processing, on the pitting corrosion resistance have been reported for 316L.[25] Blasting was found to have a detrimental effect on the pitting corrosion resistance of 316L in chloride containing solutions.[26] The duration of shot peening (blasting) was further found to play a critical role for the pitting corrosion resistance of 316L.[27] Numerous knowledge gaps exist that are related to effects of surface post-processing of 3D printed materials on the corrosion properties.[19] Available studies focus mainly on SLM-fabricated metals.[10,28–30] Knowledge on the influence of surface finish on the corrosion behavior and surface oxide characteristics of BJ printed 316L stainless steels is still not reported. The aim of this work was therefore to investigate the corrosion behavior of BJ printed 316L surfaces with and without different post surface treatments of blasting and superfinishing

*Electrochemical Society Member.
zE-mail: m.atapour@cc.iut.ac.ir; yolanda@kth.se; yhedberg@uwo.ca

treatments. Pitting corrosion resistance, surface topography, porosity, and surface oxide composition were investigated before and after exposure in diluted hydrochloric acid (HCl).

Experimental

Fabrication of binder jetting printed specimens.—AISI 316L stainless steel specimens were fabricated (printed) by Digital Metal (DM) based on their metal binder jetting additive manufacturing (AM) technology. Micron-sized spherical 316L powder (14 μm mean diameter, Digital Metal AB) was used as feedstock material and C20 ink (Digital Metal AB) was applied as binder material. The binder was fully organic. The powder was characterized by means of laser diffraction in aqueous solution, using the same method as reported previously,[31] revealing the same mean diameter (14 μm) as given by the supplier. The magnetic properties of the powder were investigated by means of a strong magnet, which was moved against gravity outside of the vessel containing the powder.[32] Parallel measurements were performed on wrought 316L coupons (thickness 2 mm). Parts of the results of the wrought reference material have recently been published as a reference for SLM 316L specimens[7] and are included for comparative reasons. The chemical compositions of the printed and the wrought specimen, based on supplier information, are given in Table I. The printed specimens (5 × 10 × 1 mm) were fabricated using optimized industrial parameters for 316L. Printing was performed in a DMP2500 printer with layer thickness 42 μm and print speed of 100 cm^3 h^{-1}. Components were separately de-bound at 345 °C for 2 h prior to sintering. The sintering process was conducted at 1370 °C for 2 h in hydrogen atmosphere. According to Digital Metal AB, the binder is completely removed during the de-binding and sintering processes.

After sintering, two third of the specimens were subjected to sand blasting and subsequently one third (half of the sand blasted) specimens were processed through a superfinishing process. The blasting process was performed with blasting media MSEKR 54 A at 3 bar pressure for a period of 5–10 s or until an even blasted surface was obtained. The blasting media had a particle size of 260–340 μm and was supplied by Iepco AG, Switzerland. Superfinished components were treated with the ISF® process by REM Surface Engineering, US. The process is a two-stage water-based chemical-mechanical process. The first (refinement) stage was performed in a solution of Magalloy® Mag2300 for a period of 4 h. The second (burnish) stage utilized Ferromil® FBC-295 for 8 h.

After sintering, the surface roughness was, based on supplier information, approximately 6 μm, followed by post-blasting to 3 μm, and super-finishing to 1 μm. The characteristics of these surfaces, the as-sintered, the as-blasted and the as-superfinished, were investigated and compared.

Microstructural characterization of printed and wrought surfaces.—The microstructures were characterized using light optical microscopy (LOM, a Leica DM2700 M instrument) and scanning electron microscopy (SEM, a tabletop TM-1000 Hitachi microscope). The surface morphologies of the different printed specimens were investigated in their as-received conditions by means of LOM.

The surfaces of the wrought specimen and one of the as-sintered printed specimens were abraded using 1200 grit SiC paper, polished using a polishing cloth with 6 followed by 1 μm diamond paste,

subsequently, ultrasonically cleaned in ethanol for 5 min, and finally dried with nitrogen gas at room temperature. The polished wrought and as-sintered specimens were then etched using Kalling's No. 2 reagent (50 ml HCl, 50 ml ethanol, and 2 g cupric chloride powder in a 100 ml solution) at room temperature for 30 s prior to the microstructural investigation by means of LOM.

In order to investigate the presence of inclusions in the specimens, the as-sintered and wrought 316L specimens were also characterized using SEM equipped with an energy dispersive X-ray spectrometer (EDS). The specimens were polished and cleaned similar as described for the microstructural investigation but without the etching step.

The microstructural phase composition was assessed using X-ray diffraction (XRD, Philips X'Pert-MPD, the Netherlands) with Cu Kα radiation (λ = 0.542 Å). Phase analysis was conducted by X'Pert High Score software.

Surface characterization of as-received BJ printed and wrought surfaces.—The surface topography of the wrought (abraded, 1200 grit SiC) and as-received BJ printed specimens with different surface finish were determined using a Bruker, DekraXT, surface profilometer with Vision64 software. The scan range was 65.5 μm with a tip radius of 2 μm. The vertical resolution was 10 nm. The dimension of the examined area was 2 × 2 mm^2. Different parameters of Ra (arithmetical mean deviation of the assessed profile), Rp (maximum peak height of the profile), Rq (root mean square average of the profile), Rv (maximum valley depth) and Rz (maximum height of the profile) were determined based on ISO 4287 standard.[33]

The surface wettability of all specimens, for as-received printed surfaces and abraded (1200 grit SiC) surface for the wrought 316L, was assessed by recording the static contact angle (θ) between the surface and a 2 μl droplet of ultrapure water (18 MΩ cm) at ambient temperature, atmospheric pressure and a relative humidity of about 45%. The contact angle of the water droplet was measured using an optical measurement system (CA-500A, Sharif Solar, Iran) with a goniometer software tool in a static mode. These tests were repeated five times for each specimen. Prior to examinations, the surfaces were blown with air to avoid static electricity. A surface with a contact angle exceeding 90° is considered hydrophobic, and hydrophilic if the angle is lower than 45°.[34]

Surface compositional analyses of the outermost surface (5–10 nm) were performed by means of X-ray Photoelectron Spectroscopy, XPS (Kratos Analytical, Manchester, UK, monochromatic 150 W, Al X-ray source, UltraDLD spectrometer). Measurements were performed on duplicate locations (300 × 700 μm) for each specimen (abraded wrought 316L, as-received BJ printed specimens), and for all specimens exposed for one week in diluted HCl. Wide spectra and high-resolution spectra (pass energy of 20 eV) were obtained for Fe 2p, Cr 2p, Ni 2p, Mn 2p, Cl 2p, O 1 s, and C 1 s (as an energy reference, 285.0 eV).

Whether differences were statistically significant or not was determined by means of a student's t-test of unpaired data with unequal variance (Kaleidagraph v. 4.0), with $p < 0.05$ referred to as a statistically significant difference. Despite different surface roughness for the different surfaces, there was a minor effect of the surface roughness on the intensity of the peaks. To account for any surface roughness effect, the results are presented as relative ratios of metallic and oxidized peaks of the different metals.

Table I. Nominal bulk composition (wt-%) of the 316L binder jetted and of wrought AISI 316L used as reference material based on supplier information.

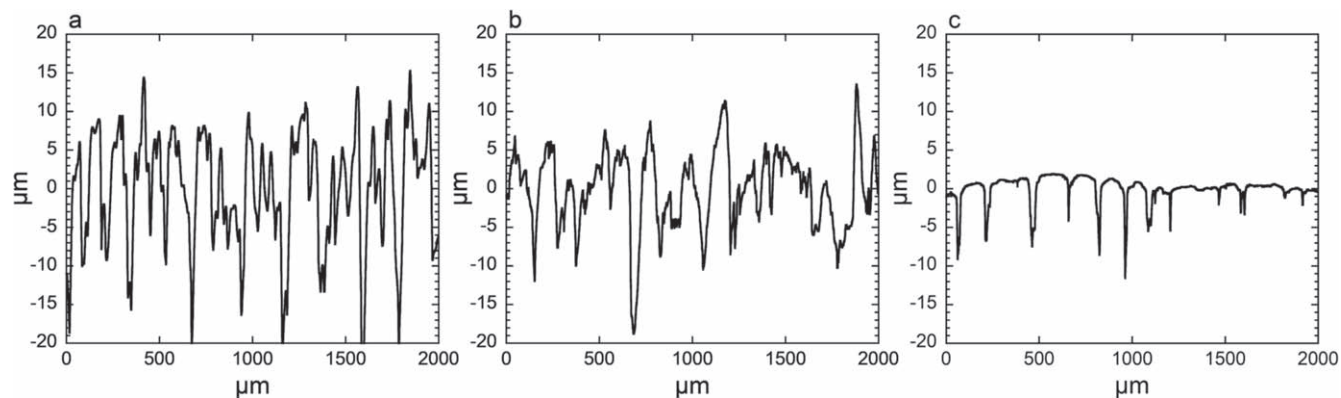| 316L	Cr	Mn	Ni	Cu	Mo	N	C	S	Fe
As-sintered	17.5	1.2	11.9	N/A	2.2	0.004	0.02	0.001	Bal.
wrought	16.9	1.3	10.1	0.5	2.0	0.05	0.02	0.0006	Bal.

N/A—no data available.

Figure 1. Representative surface line profiles of the surface topography of the BJ printed 316L specimens of different post surface treatment: as-sintered (a), as-blasted (b), and as-superfinished (c).

Electrochemical measurements and immersion test.—Electrochemical characterization, including open circuit potential (OCP), potentiodynamic polarization, and electrochemical impedance spectroscopy (EIS) evaluations, were accomplished at aerated conditions and room temperature using a Princeton Applied Research potentiostat equipped with several PMC-1000 channels. All corrosion tests were conducted in diluted HCl [pH 1.5, 4 g l^{-1} 25% HCl solution (3.6 ml l^{-1}) in ultrapure water (18.2 MΩ cm resistivity, Millipore, Sweden)] using a conventional three-electrode flat cell with the specimens (exposed area 1 cm^2) as working electrode, a platinum mesh as counter electrode and an Ag/AgCl saturated KCl electrode as reference electrode. Before the corrosion experiments, the as-received printed specimens were ultrasonically degreased in ethanol and acetone for 5 min in each, subsequently, rinsed by ultrapure water, and dried with nitrogen gas (at room temperature). The wrought specimen was abraded with 1200 grit SiC paper and then cleaned as described for the printed specimens. All specimens were prior to the electrochemical measurements stored for 24 ± 1 h in a desiccator (room temperature) to ensure a reproducible surface oxide.

OCP assessments were conducted for 1 h before all other corrosion evaluations to ensure a steady state condition. Cyclic polarization was carried out with a scan rate of 1 mV s^{-1} from −0.25 V vs OCP to 1.2 V vs Ag/AgCl sat. KCl or when the current reached 0.1 mA cm^{-2}, followed by a reverse scan back to the measured corrosion potential. To avoid crevices, the samples were tested with standard flat cells equipped with sealing rings. After each corrosion test, the surface of the specimen was observed by LOM for crevice corrosion along these sealing rings (none was found).

EIS was performed at OCP by applying an alternating current (AC) voltage with an amplitude of 10 mV_{rms} and sweeping the frequencies from 10,000 Hz to 0.01 Hz.

Based on literature findings of EIS fitting of SLM and wrought 316L,[7,35–37] the EIS data was fitted (ZView software) using a one-time constant equivalent circuit (simplified Randles circuit). In this model, R_s and R_p represent the electrolyte resistance and the polarization resistance, respectively. The constant phase element (CPE) represents the double layer capacitance of the interface, which has non-ideal characteristics resulting from surface heterogeneity, roughness, edge effects, etc. The impedance of the CPE (Z_{CPE}) is defined as $Z_{CPE} = 1/(Q(j\omega)^n)$, where Q is the CPE parameter, j is the imaginary unit ($j^2 = -1$), ω is the angular frequency and n ($0 \leqslant n \leqslant 1$) is the phase constant exponent, which is related to the roughness, porosity, and physical nature of the metal surface.[38] CPE is representative of a pure capacitor when n = 1, and of a pure resistor when n = 0. A good fitting of the experimental data was achieved based on the fitting quality evaluations with chi-squared ($\chi 2$) values lower than 0.007.

Immersion tests were conducted in the diluted HCl solution at room temperature for all specimens, surface-prepared as above, for 168 h (one week). After immersion, the coupons were rinsed with ultrapure water and evaluated using SEM and XPS. All test vessels were acid-cleaned (10% HNO_3 for at least 24 h, rinsed 4 times with ultrapure water and dried in ambient air in the laboratory).

Results

Surface topography.—The surface profiles of the different BJ printed 316L specimens are shown in Fig. 1. The as-sintered specimen exhibited the highest roughness (Ra of 6.3 ± 0.4 μm) compared with the as-blasted (4.3 ± 0.8 μm, a decrease of 32%) and the as-superfinished specimens (0.88 ± 0.45 μm, a decrease of 86% as compared to as-sintered). As shown in Fig. 2, the maximum profile peak height (Rz) of the as-sintered specimen was 37 ± 4.4 μm, which is significantly higher as compared to that of the as-blasted (26 ± 4.8 μm) and as-superfinished (10 ± 3.0 μm) specimens. Compared to the blasting process, the superfinishing treatment reduced all surface texture parameters even further (Fig. 2). The blasting and superfinishing treatments exhibited different impacts on the surface texture of the BJ printed 316L. The influence of the superfinishing process on Rp (1.3 μm as compared to 13.3 μm for the as-sintered) was higher than on Rv (8.7 μm as compared to 24 μm), however, the blasting process had a smaller effect on the peaks (Rp = 9.8 μm) and valleys (Rv = 16 μm), Fig. 2.
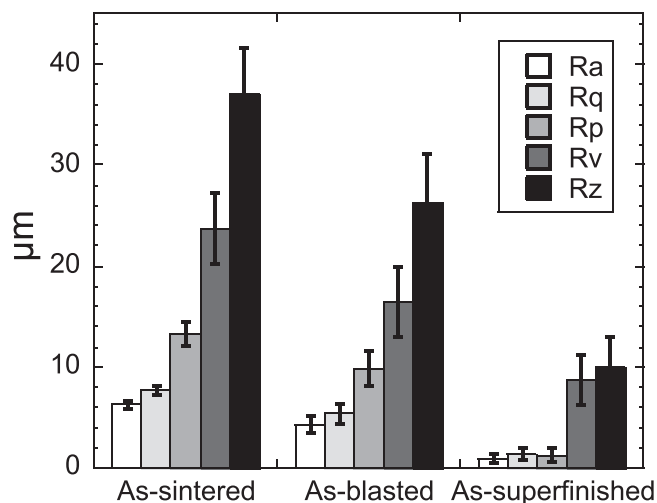

Figure 2. Surface texture parameters of the BJ printed 316L with different surface finishing processes. The error bars show the standard deviation of triplicate measurements. Ra (arithmetical mean deviation of the assessed profile), Rp (maximum peak height), Rq (root mean square average of the profile), Rv (maximum valley depth) and Rt (maximum height of the profile).
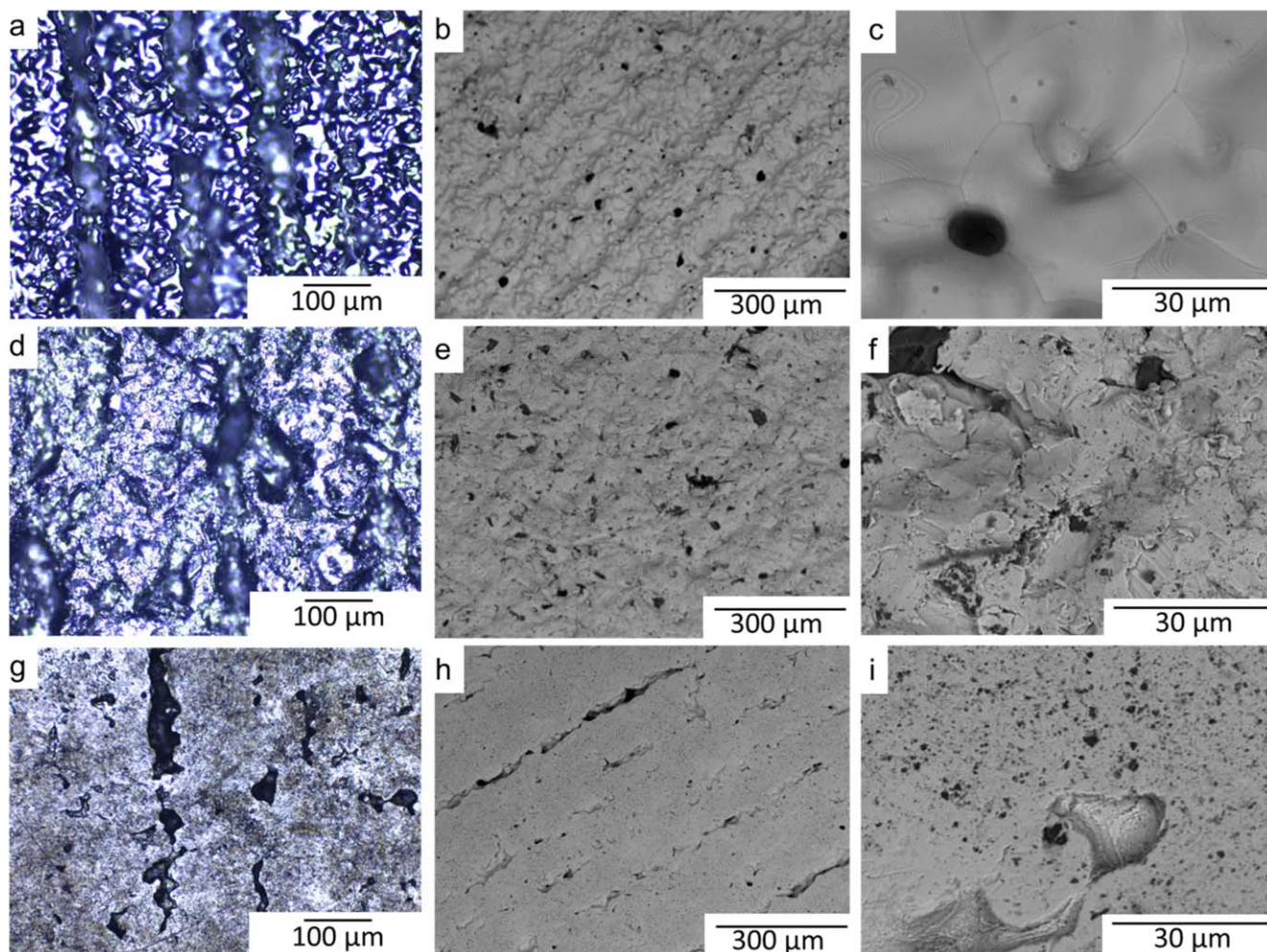
Figure 3. Light optical (left) and scanning electron micrographs (middle and right columns) of the surface morphology of the BJ printed 316L surfaces at different magnifications: (a)–(c) as-sintered, (d)–(f) as-blasted, (g)–(i) as-superfinished.

Microstructure and surface topography of BJ printed and wrought 316L.—Optical and SEM imaging of the as-received printed specimens revealed heterogeneous surfaces with closed cavities, printing traces, and remaining sticky powders, Fig. 3 and Fig. S1 (available online at stacks.iop.org/JES/167/131503/mmedia).

Some metallic agglomerates were visible on the as-sintered surface (Fig. S1) showing a relatively dense and rough surface with pores. The printing tracks were well-arranged and parallel to the printing direction with visible coherent bonding features between these tracks. No apparent cracks or large-sized pores were observed on the as-sintered surface, although some micropores were visible. The blasting process resulted in an irregular and rough surface with crater-like regions, Fig. 3. The presence of sharp edges and furrows on the as-blasted surface was attributed to plastic deformation and material tearing associated with the blasting treatment,[39] surface features that were removed by the superfinishing treatment, Fig. 3. The presence of some pores and cavities, Figs. 3 and S1, is probably related to the BJ AM method applied, as a density of 97% is expected for the process used for this study.

The LOM investigation of the wrought and etched 316L specimen showed fine equiaxed grains (mean grain size: 8 μm) with some annealing twins, Fig. S2. Detailed microstructural analysis of the 316L material is reported elsewhere.[40] A similar investigation on the BJ printed specimen (polished and etched as-sintered 316L) revealed larger grains (50–100 μm as compared to 5–30 μm for the wrought specimen) and also twins, Fig. S2. Based on optical image analysis (Image J software) the surface porosity of

the BJ printed specimens was estimated to 39.5 ± 3.2% (as-sintered), 35.4 ± 2.3% (as-blasted) and 18.2 ± 1.9% (as-superfinished).

The majority of the powder was found to be ferromagnetic, which indicates a rapid solidification process causing a metastable body-centered cubic (BCC) ferritic phase,[32,41] which upon heating can be transformed to its stable austenitic phase. XRD patterns of the wrought and the printed and sintered surfaces are presented in Fig. 4. All specimens exhibited the face-centered cubic austenite phase (FCC-γ) with strong diffraction peaks corresponding to crystal faces of (111), (200), and (220). The peak intensity of the (220) crystal face was stronger for the wrought specimen compared to the printed specimens, whereas the opposite was the case for the (111) crystal face. No traces of the BCC ferrite phase were observed for any of the specimens.

To evaluate the presence and distribution of inclusions, SEM and EDS analyses were carried out. As shown in Figs. 5a–5b, the inclusions were mostly spherical in shape for the wrought 316L surface. The EDS analyses of these inclusions revealed excess oxygen, magnesium, aluminum, manganese, titanium, and/or calcium, Fig. S3. No evidence of MnS inclusions was found, probably due to the very low sulfur content of this wrought 316L. These observations are in agreement with previous findings.[42] The SEM micrographs of the polished as-sintered specimen (Figs. 5c–5d) revealed a microstructure with random-sized porosity as the main microstructural feature.[12] No evidence of any inclusions was observed for the BJ polished and etched as-sintered 316L specimen, and no sulfur, calcium, aluminum, titanium, or magnesium were detected, Fig. S3.
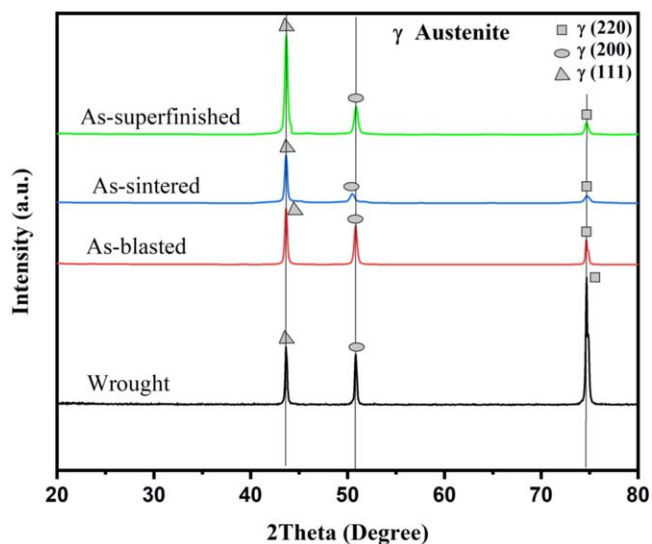
Figure 4. XRD diffraction patterns of the microstructure of the BJ printed specimens of different post-treatments and wrought 316L for comparison.

Electrochemical properties.—Both the as-sintered and the as-superfinished specimens exhibited a more positive open circuit potential, OCP, after 1 h in diluted HCl ($\approx$0.05 V$_{Ag/AgCl}$) compared to the as-blasted and the wrought 316L specimen ($\approx$ −0.1 V$_{Ag/AgCl}$), Fig. 6a. The OCP decreased during the first 1000 s followed by relatively stable potentials for the as-sintered and the

as-superfinished specimens. In the case of the as-blasted and the wrought specimens, OCP gradually increased with time (some extent of passivation).

Cyclic potentiodynamic polarization measurements showed a passive behavior of all specimens in the diluted HCl solution (pH 1.5), Fig. 6b, Table II. The passive current density was higher for the printed surfaces as compared to the abraded wrought 316L reference, Table II. The as-blasted surface showed the narrowest passive region and the lowest pitting potential (E$_{pit}$) value compared with the as-sintered and the as-superfinished surfaces that exhibited wider passive regions and high pitting potentials. While the pitting corrosion resistance was improved by the superfinishing process, the blasting treatment strongly deteriorated the same property.

The as-sintered and the as-superfinished surfaces did not reveal any current fluctuations prior to the breakdown potential, effects observed for the as-blasted and the wrought specimens, Fig. 6b. In contrast to these observations, the repassivation behavior was impeded for all printed specimens compared to the wrought material.

EIS measurements were performed to further characterize the surface oxide properties of the printed specimens. The Nyquist plots, Fig. 7, revealed similar capacitance arc shapes for all the specimens. Generally, the barrier properties of the passive oxide increase with increasing radius of this capacitive arc.[44] The surface barrier properties (radius) decreased in the following way: as-superfinished > as-sintered > wrought > as-blasted specimens, Fig. 7.

All negative phase angles evolved between 50 and 60° in the Bode plots, Fig. S4, which means that the passive oxide had mainly capacitive properties.[45] The impedances at intermediate and low frequencies represent the charge transport characteristics across the double layer and the passive oxide film, respectively.[46] Observed shifts of the response in the Bode plots to higher impedance/phase
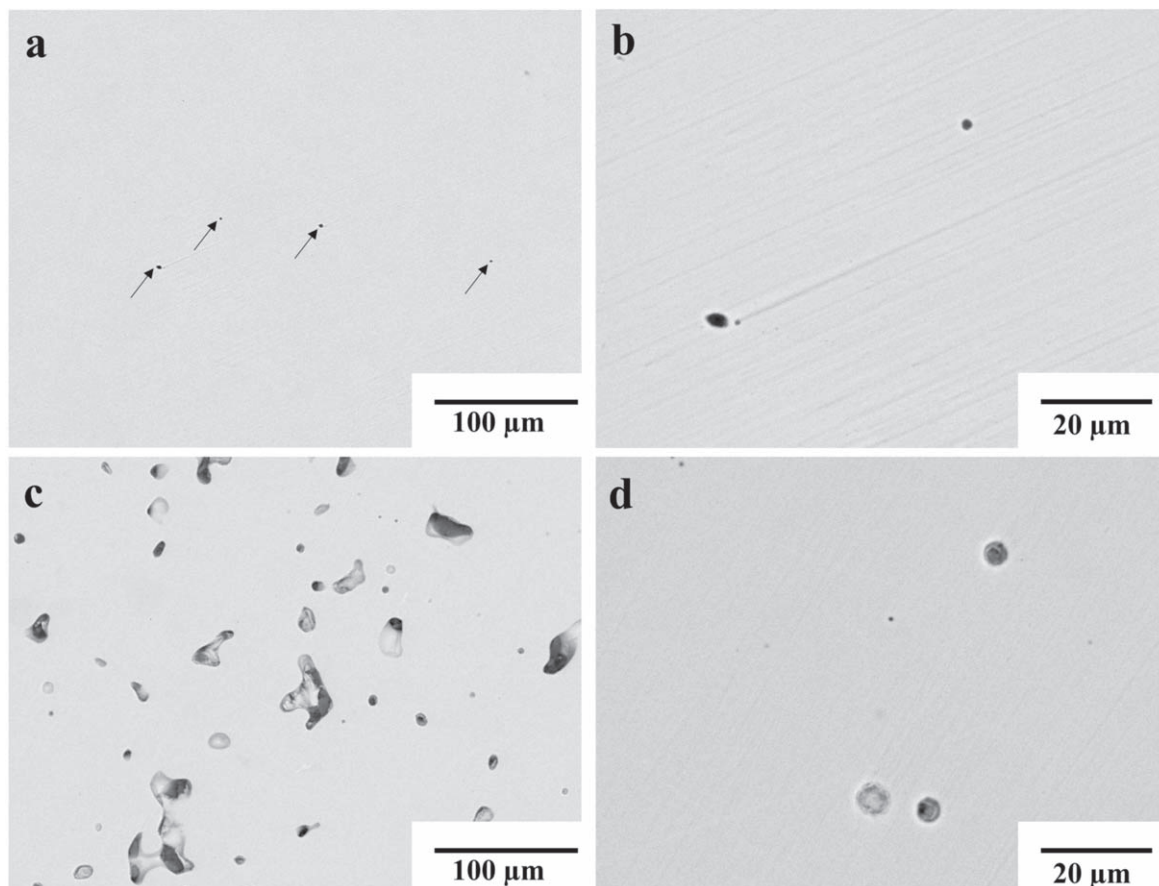

Figure 5. SEM images of polished wrought (a)–(b) and BJ as-sintered (c)–(d) 316L specimens. The arrows in (a) indicate inclusions. Higher magnifications in (b) and (d).
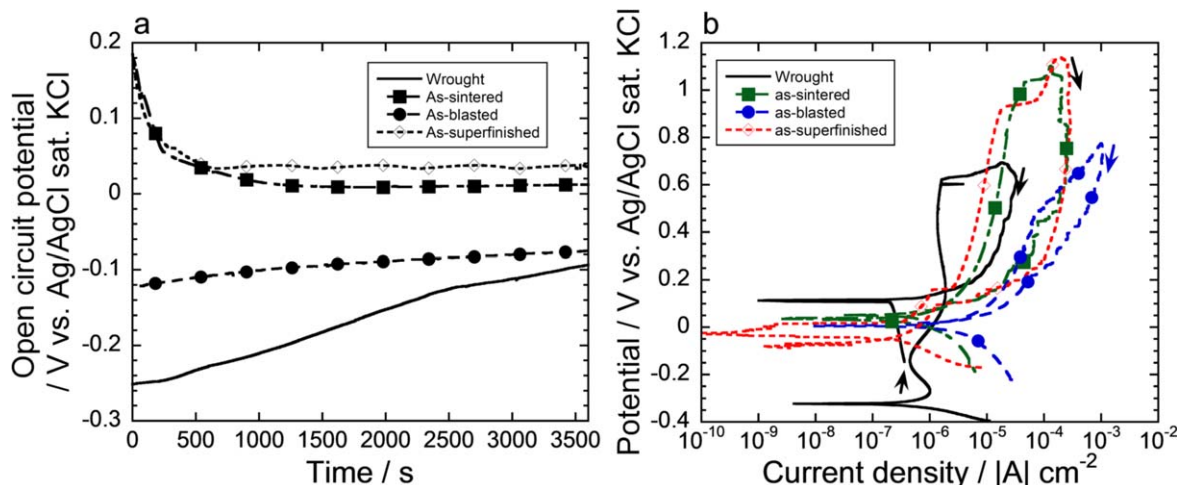
Figure 6. (a) Open circuit potential (OCP) measurements with time for the BJ printed 316L specimens of different post treatments compared with wrought 316L for comparison in diluted HCl solution (pH 1.5) at room temperature up to 1 h. The data reflects the mean value of triplicate measurements of unique specimens. (b) Representative cyclic polarization curves (forward and reverse scans). The markers in (a)–(b) are only guides for the eye. The arrows in (b) mark the scan direction.

Table II. Electrochemical results: corrosion potential (E_{corr}), corrosion current density (i_{corr}), passive current density (i_{pass}), pitting potential (E_{pit}) and repassivation potential (E_{rep}), obtained from the cyclic potentiodynamic polarization curves of printed and wrought 316L specimens immersed in diluted HCl solution for 1 h (pH 1.5) at room temperature. The passive current density was determined from the center of each passive range[43] and the corrosion current density and corrosion potential by Tafel approximation. Each parameter is based on measurements for at least three replicate measurements showing the mean and standard deviations.

Specimens	i_{corr} (μA cm^{-2})	E_{corr} (mV$_{Ag/AgCl}$)	i_{pass} (μA cm^{-2})	E_{pit} (mV$_{Ag/AgCl}$)	E_{rep} (mV$_{Ag/AgCl}$)
Wrought 316L	0.7 ± 0.1	−323 ± 35	2 ± 1	607 ± 20	150 ± 15
As-sintered	0.5 ± 0.2	27 ± 5	15 ± 8	1003 ± 210	−125 ± 16
As-blasted	2 ± 0.5	3 ± 0.5	40 ± 3	407 ± 30	−30 ± 8
As-superfinished	0.1 ± 0.02	−24 ± 3	11 ± 5	965 ± 120	97 ± 10

angle values indicate improved electrochemical stability of the passive oxide.[47] The blasting treatment resulted in a reduction of the negative phase angle values (reduced chemical stability),

Figure 7. Electrochemical impedance measurements of the BJ printed 316L surfaces of different surface treatment illustrated by representative Nyquist plots and equivalent electrical circuit (EEC) model (inset) in diluted HCl (pH 1.5). Corresponding Bode plots are shown in Fig. S4.

whereas improved stability of the surface oxide was evident for the as-sintered and as-superfinished specimens (based on their higher negative phase angle values in a wider frequency range).

A higher corrosion resistance is associated with a larger value of R_p since the corrosion current density is inversely related to R_p based on the Stern–Geary equation.[48] The lowest corrosion resistance (R_p), and therefore the highest corrosion rate, was observed for the as-blasted specimen, Table III. The as-superfinished specimen showed the highest corrosion resistance, being approximately 4-fold higher compared with the as-blasted specimen, Table III. The as-blasted specimen exhibited the highest CPE, Table III. An increased CPE can be attributed to a reduced thickness of the passive layer (surface oxide).[49]

Corrosion morphologies and surface characteristics after one week of immersion in diluted HCl.—From the SEM images of the printed surfaces after one week of immersion at the open circuit potential it was evident that no pitting could be observed within the pores of either the as-sintered, the as-blasted, or the as-superfinished specimens, Figs. 8c–8h, whereas there was evidence of pitting for the wrought specimen observed from preferential attacks adjacent to the relatively large-sized irregularly shaped inclusions, Figs. 8a–8b. These pits adjacent to the inclusions in the wrought specimen occurred at open circuit potential after one week of exposure, despite a high pitting potential and repassivation potential of abraded wrought 316L determined initially, Table II. It is, however, not possible to judge from the SEM images in Figs. 8a–8b, whether these pits have re-passivated.

The surface wettability and the extent of hydrophobicity have been shown to be closely related to surface topography, surface roughness, chemical properties, surface energy and texture, and hence influence
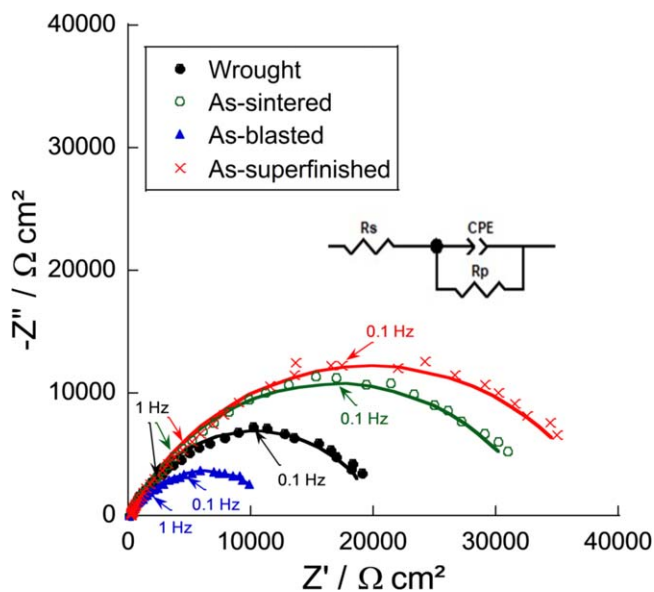
Table III. Fitted electrochemical elements of experimental EIS spectra for BJ printed specimens of different post-treatment and abraded and aged wrought specimens immersed in diluted HCl for 1 h. The results reflect at least two, and at most five, replicate measurements showing mean and standard deviations.

Specimen	R_S (Ω cm^2)	CPE (s^n Ω^{-1} cm^{-2})	n	R_p (kΩ cm^2)	χ^2 ($\times 10^{-3}$)
Wrought	183 ± 15	45.8 ± 1.1	0.75 ± 0.01	20.8 ± 5	<7
As-sintered	172 ± 5	42.5 ± 1.5	0.75 ± 0.05	43.0 ± 8	<5
As-blasted	166 ± 12	140 ± 12	0.74 ± 0.01	11.3 ± 3	<2
As-superfinished	179 ± 8	59.1 ± 0.50	0.81 ± 0.02	44.9 ± 5	<3

the surface reactivity and the extent of corrosion.[34,50] In accordance with the profilometry investigation (Fig. 1), the static water contact angles decreased as follows: as-blasted (111°) ≈ as-sintered (107°) > wrought (83°) > as-superfinished (44°), Fig. S5 (supplementary material).

X-ray photoelectron spectroscopy, XPS, was conducted to quantify the oxidized metal content of the outermost surface of the printed and the wrought specimens. The wrought specimen has been abraded and then stored for 24 h in a desiccator, while the printed specimens were investigated as-received, stored in a desiccator for about three months prior to testing. Metallic peaks of Fe, Cr and Ni (2p$_{3/2}$: Fe: 707.4 ± 0.4 eV, 708.3± 0.1 eV; Cr: 574.4 ± 0.4 eV; Ni: 853.1 ± 0.3 eV[51]) were observed for all surfaces, Fig. 9, which indicate a thickness of the surface oxide less than 5–10 nm (the information depth). The relative oxide to metal peak fraction of the as-superfinished specimen was slightly higher (0.94–1) compared with the same fraction of the other as-received printed specimens and the wrought reference (0.85–0.89), though not statistically significant. These findings imply a possible thickening of the surface oxide as a result of the superfinishing process. The as-superfinished surface also revealed a larger relative enrichment of trivalent chromium, Cr$_{ox}$/(Fe$_{ox}$ + Cr$_{ox}$) 35%–37% as compared to 17%–23%, within the surface oxide (Cr 2p$_{3/2}$: 576.8 ± 0.4 eV, 578.2 ± 0.4 eV) compared with observations made for both abraded wrought and the other as-received printed surfaces (p < 0.05), Fig. 9. Immersion in diluted HCl (pH 1.5) for one week resulted in the enrichment of trivalent chromium relative to iron (Cr$_{ox}$/(Fe$_{ox}$ + Cr$_{ox}$): 39%–59% as compared to 17%–37%, p < 0.05) and reduced surface oxide thicknesses (oxide to metal peak fraction: 0.70–0.85 compared to 0.85–1, only statistically significant for the wrought 316L specimen, p < 0.001) for all surfaces (Fe 2p$_{3/2}$: 710.6 ± 0.9 eV, 713.0 ± 0.9 eV), Fig. 9. Nickel was only observed in its metallic state and enriched within a layer (Ni$_{met}$/(Ni$_{met}$ + Cr$_{met}$ + Fe$_{met}$) ratio: 24 wt% compared to its bulk content: 10%) adjacent to the surface. Evident peaks of carbides (283.3 ± 0.2 eV) were observed for all printed surfaces.

Discussion

Effects of surface topography, surface roughness, wettability and surface composition.—The BJ printed 316L specimens with different surface treatments showed large differences in terms of surface topography, roughness, and wettability, properties that were mainly attributed to the presence of some manufacturing defects and effects, such as open pores, remaining sticky powders, redeposited powders, spattering powder particles, and printing traces. Generally, powders with a high flowability result in a smoother surface of the printed part.[12] Effects of the re-use of non-printed powder during multiple printing processes and of any intermediate powder cleaning treatments remain to be investigated in future studies.

The surface roughness has been shown to be a critical factor for the pitting corrosion susceptibility of stainless steels in chloride containing solutions.[52] A smoother surface finish is generally associated with a lower pitting susceptibility due to the reduction of the number of active sites that could act as sites of pit initiation.[53]

The surface roughness of the as-sintered printed specimen (Ra = 6 ± 0.4 μm) was significantly lower than reported for as-printed SLM specimens (10–30 μm).[18] This might be an effect of the BJ technique, which is a solid state 3D printing technique performed at

room temperature and for which the surrounding powder provides enough support during the printing process. This facilitates de-powdering and reduces the surface roughness of the printed surface. The post-superfinishing process largely reduced the surface roughness and increased the surface wettability. Observations of the static water contact angle for the wrought specimen agreed with previously reported findings for polished AISI 304 stainless steel.[54] The low contact angles observed for the as-superfinished specimen, which underwent a chemical-mechanical two-step superfinishing process, could possibly be attributed to effects of the residues (from e.g. acids or complexing agents) of the superfinishing process, as previously reported for wrought 304 treated with either nitric or citric acid.[54]

Findings of the surface roughness/wettability were linked to the observations related to the electrochemical characteristics of the printed materials, see below. The XPS investigation clearly showed similar composition of the outermost surface oxide of the printed specimens compared with abraded wrought material of 316L. These similarities are in sharp contrast to findings observed for as-received SLM printed 316L, reported to comprise oxidized manganese as a result of the rapid solidification process.[7,55] A reduced thickness of the surface oxide was observed for all specimens after exposure in diluted HCl. This observation agrees with literature findings[43,56,57] as well as the observation of the enrichment of nickel adjacent to the surface oxide.[58]

Effects of surface treatment.—Mechanical post-processes like sanding, polishing, and burnishing have been reported to strongly alter the surface roughness and residual stresses of 316L stainless steels.[59] The blasting process can induce a highly deformed surface layer with fragmented grains, dislocations, and residual stresses, and therefore, deteriorate the pitting resistance, as observed for the BJ printed specimen in this study. Negative effects on the pitting corrosion of SLM 316L by grinding has been shown to include tensile residual stresses that reduce the resistance to pitting corrosion.[60] However, the as-blasted BJ printed specimen of this study showed an improved pitting corrosion performance during 168 h immersion in diluted HCl as compared to its wrought counterpart.

The as-superfinished BJ printed specimen showed clearly improved pitting corrosion resistance compared to the as-blasted specimen. This suggests that this treatment might outweigh the negative effects of the blasting treatment on the pitting resistance in several ways: (i) it clearly reduced the surface roughness, (ii) it induced chromium enrichment at the outermost surface, and (iii) it might have reduced some of the surface stresses induced by the blasting process. The as-superfinished surface treatment did furthermore result in a reduced level of surface porosity.

Similarities of the SLM and BJ printed AM technologies.—The absence of micrometer-sized inclusions, as observed in this study for the BJ printed specimens has also been reported for SLM 316L specimens.[6] However, the reasons are different. While rapid solidification during the SLM process is the main reason for the absence of these conclusions,[61–63] the reason for the BJ printed specimens is most probably related to the quality of the input feed powder. In this study, it was evident that the spherical gas-atomized 316L powder particles were relatively small (mean value of 14 μm) and largely ferromagnetic, which indicates a rapid solidification process according to literature findings.[32,41,64] Ferromagnetic 316L
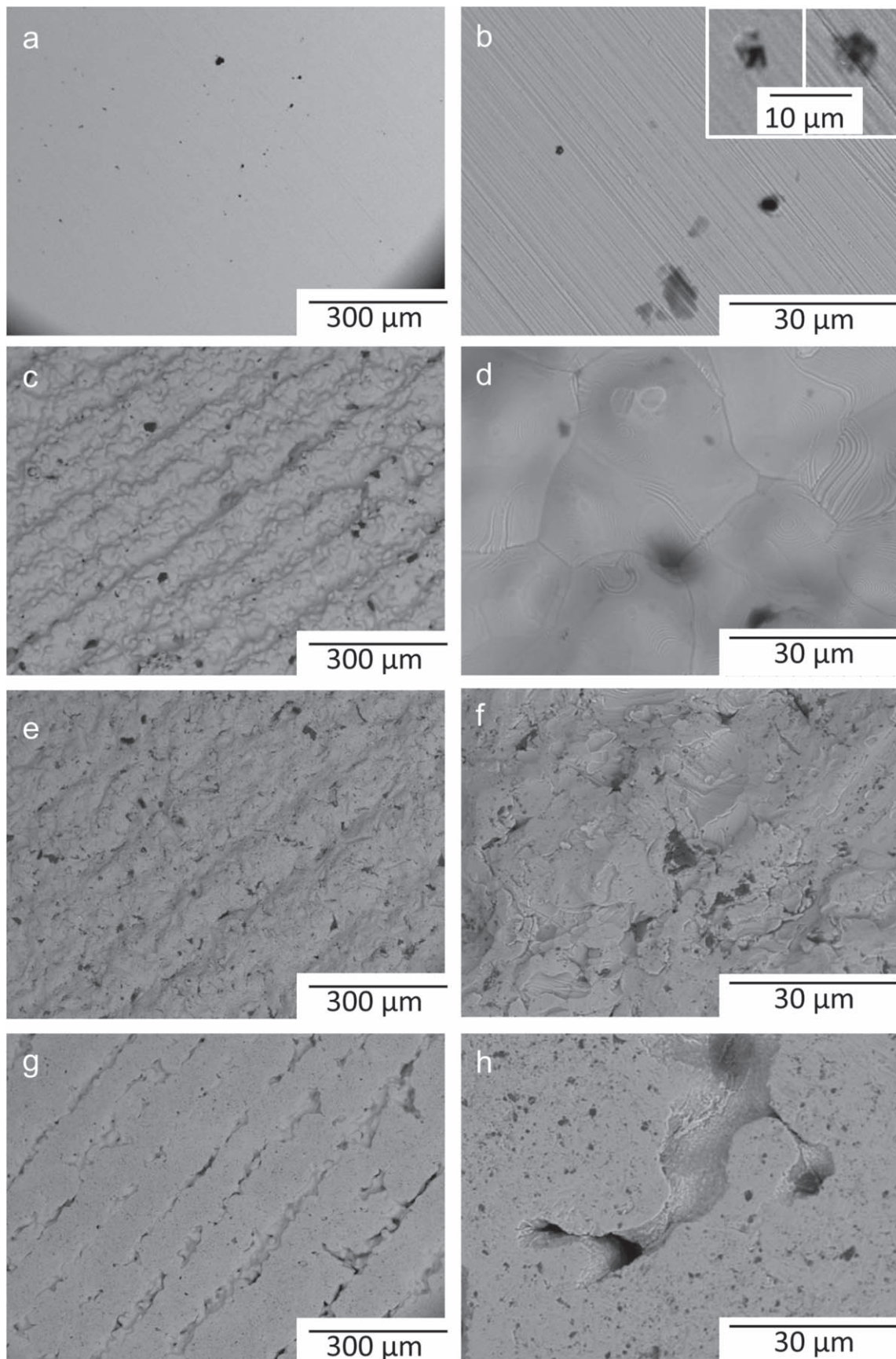
Figure 8. SEM images at low (left) and high (right) magnification after one week immersion in diluted HCl solution (pH 1.5) at room temperature for BJ printed and wrought 316L surfaces: (a)–(b) wrought (c)–(d) as-sintered printed, (e)–(f) as-blasted printed, and (g)–(h) as-superfinished printed specimens. The inset in the upper right image (wrought 316L) shows pits at higher magnification.

Figure 9. Relative mass composition of nickel, iron, and chromium in their metallic and oxide states, excluding carbon and oxygen, at the outermost (5–10 nm) surface of BJ printed (of different surface treatments) and wrought 316L as determined by XPS. Surface conditions: abraded wrought (after 24 h storage in a desiccator), as-received (after months of storage in a desiccator) printed specimens, and abraded (wrought) and as-received (printed) surfaces after immersion in diluted HCl for one week at room temperature. Nickel was only detected in its metallic form. No manganese was observed.

gas-atomized powders, showing a body-centered cubic non-equilibrium phase, have previously been observed for particle sizes around 10 μm and below and are characterized by a single-crystalline phase, a close to amorphous surface oxide, less pitting corrosion susceptibility, and no inclusions.[32,41,64] The reason is the very high solidification rate and undercooling during the atomization process for these small particles.[65,66] It has previously been suggested that larger-sized (>40 μm) gas-atomized 316L particles solidify with oxide inclusions and at least partially crystalline surface oxides,[32,66] while the very rapid solidification of the smaller sized gas-atomized 316L particles causes amorphous, inclusion-free, surface oxides, and a thermodynamically unstable ferritic bulk crystal structure.[32,41,64] Rapid solidification from the molten phase has also for other processes, such as laser surface melting, been associated with the reduction of inclusion sizes and their dissolution.[67,68] This would suggest that the feed powder quality is of higher importance to the BJ AM process as compared with the SLM AM process. The absence of inclusions in the BJ specimens is probably a major reason for the higher pitting corrosion resistance observed after one week of immersion and large/comparable passivity ranges as compared to the wrought specimen investigated in this study.[7,69]

A BJ printed specimen still consists of some porosity when compared to the specimens produced using the SLM technique that can result in a nearly completely dense material, findings observed also in this study. However, it was also shown that the extent of surface porosity is strongly influenced by the post-treatment. This was supported by hardness measurements (Fig. S6, supplementary material). The porosity did not, in compliance with the literature,[6,45,47,70] have a significant influence on either the pit initiation, pitting potential, corrosion potential, or corrosion current density. No pitting corrosion was observed in diluted HCl (pH 1.5) after one week of immersion at OCP for any of the BJ printed specimens. These observations were in contrast to the wrought counterpart showing some pitting corrosion, effects also reported in the literature.[46] To the best of our knowledge, there is no study available that investigated the effect of porosity on corrosion of BJ printed 316L specimens. Such studies do exist for SLM specimens.[37] Similar to the findings of the BJ printed surfaces reported in this study, the SLM specimens displayed a superior pitting corrosion resistance compared with wrought specimens, despite some porosity.[47,63] The porosity most likely influenced the possibility of the BJ printed specimens to re-passivate after stable pitting, however, this requires future studies.

Final considerations.—The relatively low/comparable pitting susceptibility and the chromium-rich and dense surface oxide of the as-superfinished BJ printed 316L specimen make the printed material a possible candidate of higher or equivalent quality from a corrosion perspective compared to traditionally wrought massive surfaces of 316L. One of the main advantages of the BJ printing process, in addition to relatively low costs, is that this AM technique is carried out in solid state and at room temperature. This avoids the formation of gas voids and solidification shrinkage, which are challenges for the SLM process.[71] However, shrinkage takes place during the sintering step and the porosity is higher compared to SLM printed parts. The superfinishing treatment can improve the corrosion performance of the BJ specimens, but it can be an expensive and complicated process for complex shapes. The BJ 316L specimens in this study further showed a slightly higher pitting corrosion susceptibility as compared to abraded SLM 316L specimens investigated under similar conditions in a recent study.[7] Still, the advantage of AM parts with small-sized inclusions in the microstructure proved to be the case also for the BJ printed surfaces, most probably due to the inclusion-free input powder. Even though the possible presence of small amounts of metal carbides at the surface of the printed surfaces, as observed with XPS, these were evidently not acting as initiation sites for pitting corrosion under the experimental conditions of this study. Further studies should investigate effects of other important factors on the corrosion performance including dislocation density, evolved texture, and the size and states of the residual stress induced by the different surface treatments.

Conclusions

A BJ AM technology followed by sintering and different post surface treatments was employed to print 316L specimens (as-sintered, as-blasted, and as-superfinished) from a surface characteristics and electrochemical/corrosion perspective in diluted HCl (pH 1.5). Parallel comparative measurements were performed on abraded wrought 316L. The blasting and superfinishing treatment substantially reduced the surface roughness and level of surface porosity. Blasting had a detrimental effect on the pitting corrosion resistance of the printed surface. The superfinishing process induced an enrichment of chromium in the surface oxide that improved its resistance for pitting corrosion. All printed specimens showed reduced or comparable susceptibility to pit initiation and metastable pitting as compared to the wrought reference. No inclusions were found for the printed

specimens, while inclusions rich in magnesium and aluminum were found for the wrought counterpart. The absence of inclusions in the printed specimens could possibly be explained by the rapidly solidified small-sized (14 μm) particles of the gas-atomized feed powder. The pitting corrosion resistance of the as-superfinished specimen was improved compared with the wrought counterpart. Once stable pitting was induced, repassivation was hindered for all printed specimens compared with the wrought specimens.

Acknowledgments

ORCID

Yolanda S. Hedberg https://orcid.org/0000-0003-2145-3650

References

1. F. Khodabakhshi, M. H. Farshidianfar, A. P. Gerlich, M. Nosko, V. Trembošová, and A. Khajepour, *Additive Manufacturing*, **31**, 100915 (2020).
2. T. DebRoy, H. L. Wei, J. S. Zuback, T. Mukherjee, J. W. Elmer, J. O. Milewski, A. M. Beese, A. Wilson-Heid, A. De, and W. Zhang, *Prog. Mater Sci.*, **92**, 112 (2018).
3. T. D. Ngo, A. Kashani, G. Imbalzano, K. T. Q. Nguyen, and D. Hui, *Compos. Part B-Eng.*, **143**, 172 (2018).
4. B. Mueller, *Assembly Autom.*, **32**, 2 (2012).
5. A. Bandyopadhyay and S. Bose, *Additive Manufacturing* (CRC press, Boca Raton, FL) (2019).
6. G. Sander, S. Thomas, V. Cruz, M. Jurg, N. Birbilis, X. Gao, M. Brameld, and C. Hutchinson, *J. Electrochem. Soc.*, **164**, C250 (2017).
7. M. Atapour et al., *Electrochim. Acta*, **354**, 136748 (2020).
8. M. Alnajjar, F. Christien, K. Wolski, and C. Bosch, *Additive Manufacturing*, **25**, 187 (2019).
9. E. Yasa, J. Deckers, and J. P. Kruth, *Rapid Prototyping J.*, **17**, 312 (2011).
10. D. A. Lesyk, S. Martinez, B. N. Mordyuk, V. V. Dzhemelinskyi, Lamikiz, and G. I. Prokopenko, *Surf. Coat. Technol.*, **381**, 125136 (2020).
11. M. Ziaee and N. B. Crane, *Additive Manufacturing*, **28**, 781 (2019).
12. S. Mirzabaaei and S. Pasebani, *J. Manuf. Mater. Process.*, **3**, 82 (2019).
13. W. Gao, Y. Zhang, D. Ramanujan, K. Ramani, Y. Chen, C. B. Williams, C. C. L. Wang, Y. C. Shin, S. Zhang, and P. D. Zavattieri, *Comput. Aided Design*, **69**, 65 (2015).
14. D. Hong, D.-T. Chou, O. I. Velikokhatnyi, A. Roy, B. Lee, I. Swink, I. Issaev, H. A. Kuhn, and P. N. Kumta, *Acta Biomater.*, **45**, 375 (2016).
15. D. Dimitrov, K. Schreve, and N. de Beer, "Advances in three dimensional printing–state of the art and future perspectives." *Rapid Prototyping J.*, **12**, 136 (2006).
16. M. Vaezi, P. Drescher, and H. Seitz, *Materials*, **13**, 922 (2020).
17. https://www.digitalmetal.tech accessed 2020–09–04.
18. D. Bhaduri, P. Penchev, A. Batal, S. Dimov, S. L. Soo, S. Sten, U. Harrysson, Z. Zhang, and H. Dong, *Appl. Surf. Sci.*, **405**, 29 (2017).
19. D. Kong, C. Dong, X. Ni, and X. Li, *npj Materials Degradation*, **3**, 24 (2019).
20. D. Wang, Y. Liu, Y. Yang, and D. Xiao, *Rapid Prototyping J.*, **22**, 706 (2016).
21. A. B. Rhouma, H. Sidhom, C. Braham, J. Lédion, and M. E. Fitzpatrick, *J. Mater. Eng. Perform.*, **10**, 507 (2001).
22. A. Shahryari, W. Kamal, and S. Omanovic, *Mater. Lett.*, **62**, 3906 (2008).
23. M. Cieślik, W. Reczyński, A. M. Janus, K. Engvall, R. P. Socha, and A. Kotarba, *Corros. Sci.*, **51**, 1157 (2009).
24. B. Krawczyk, B. Heine, and D. L. Engelberg, *J. Mater. Eng. Perform.*, **25**, 884 (2016).
25. P. Peyre, C. Carboni, P. Forget, G. Beranger, C. Lemaitre, and D. Stuart, *J. Mater. Sci.*, **42**, 6866 (2007).
26. A. L. L. Barboza, K. W. Kang, R. D. Bonetto, C. L. Llorente, P. D. Bilmes, and C. A. Gervasi, *J. Mater. Eng. Perform.*, **24**, 175 (2015).
27. V. Azar, B. Hashemi, and M. R. Yazdi, *Surf. Coat. Technol.*, **204**, 3546 (2010).
28. X. Zhao, H. Liu, S. Li, X. Wang, Y. Sheng, P. Zhang, and W. Li, *J. Alloys Comp.*, **816**, 152667 (2020).
29. Z. Wang, Z. Liu, C. Gao, K. Wong, S. Ye, and Z. Xiao, *Surf. Coat. Technol.*, **381**, 125122 (2020).
30. M. Godec, Č. Donik, A. Kocijan, B. Podgornik, and D. A. S. Balantič, *Additive Manufacturing*, **32**, 101000 (2020).
31. X. Wang, I. Odnevall Wallinder, and Y. Hedberg, *Ann. Work Exposure Health*, **64**, 659 (2020).
32. Y. Hedberg, M. Norell, P. Linhardt, H. Bergqvist, and I. Odnevall Wallinder, *Int. J. Electrochem. Sci.*, **7**, 11655 (2012), http://www.electrochemsci.org/papers/vol7/71211655.pdf.
33. International Standard Organisation. ISO 4287, Geometrical Product Specifications (GPS)—Surface texture: Profile method—Terms, definitions and surface texture parameters (1997), https://iso.org/standard/10132.html.
34. E. Mahlooji, M. Atapour, and S. Labbaf, *Carbohydr. Polym.*, **226**, 115299 (2019).
35. M. Atapour, I. Odnevall Wallinder, and Y. Hedberg, *Electrochim. Acta*, **331**, 135428 (2020).
36. A. B. Kale, B.-K. Kim, D.-I. Kim, E. G. Castle, M. Reece, and S.-H. Choi, *Mater. Charact.*, **163**, 110204 (2020).
37. M. J. K. Lodhi, K. M. Deen, M. C. Greenlee-Wacker, and W. Haider, *Additive Manufacturing*, **27**, 8 (2019).
38. P. Córdoba-Torres, T. J. Mesquita, O. Devos, B. Tribollet, V. Roche, and R. P. Nogueira, *Electrochim. Acta*, **72**, 172 (2012).
39. M. Pereda, K. W. Kang, R. Bonetto, C. Llorente, P. Bilmes, and C. Gervasi, *Proc. Mat. Sci.*, **1**, 446 (2012).
40. M. Atapour et al., *Food Control*, **101**, 163 (2019).
41. Y. Hedberg and K. Midander, *Mater. Lett.*, **122**, 223 (2014).
42. S. Zheng, C. Li, Y. Qi, L. Chen, and C. Chen, *Corros. Sci.*, **67**, 20 (2013).
43. Y. Li, R. Hu, J. Wang, Y. Huang, and C.-J. Lin, *Electrochim. Acta*, **54**, 7134 (2009).
44. L.-C. Zhang and P. Qin, *Additive Manufacturing of Emerging Materials*, ed. B. AlMangour (Springer, Cham, Switzerland) p. 197 (2019).
45. Z. Duan, C. Man, C. Dong, Z. Cui, D. Kong, L. Wang, and X. Wang, *Corros. Sci.*, **167**, 108520 (2020).
46. N. S. Al-Mamun, K. Mairaj Deen, W. Haider, E. Asselin, and I. Shabib, *Additive Manufacturing*, **34**, 101237 (2020).
47. M. Kazemipour, M. Mohammadi, E. Mfoumou, and A. M. Nasiri, *J. Min. Met. Mat. S.*, **71**, 3230 (2019).
48. A. V. C. Sobral, W. Ristow, D. S. Azambuja, I. Costa, and C. V. Franco, *Corros. Sci.*, **43**, 1019 (2001).
49. D. de Castro Girão et al., *Mater. Sci. Eng. C*, **107**, 110305 (2020).
50. S. Jannat, H. Rashtchi, M. Atapour, M. A. Golozar, H. Elmkhah, and M. Zhiani, *J. Power Sources*, **435**, 226818 (2019).
51. M. C. Biesinger, B. P. Payne, A. P. Grosvenor, L. W. M. Lau, A. R. Gerson, and R. S. C. Smart, *Appl. Surf. Sci.*, **257**, 2717 (2011).
52. G. T. Burstein and P. C. Pistorius, *Corrosion*, **51**, 380 (1995).
53. P. Cisquini, S. V. Ramos, P. R. P. Viana, V. D. F. C. Lins, A. R. Franco, and E. A. Vieira, , *J. Mater. Res. Technol.*, **8**, 1897 (2019).
54. Y. Hedberg, M.-E. Karlsson, E. Blomberg, I. Odnevall Wallinder, and J. Hedberg, *Colloid Surf. B*, **122**, 216 (2014).
55. F. Andreatta, A. Lanzutti, E. Vaglio, G. Totis, M. Sortino, and L. Fedrizzi, *Mater. Corros.*, **70**, 1633 (2019).
56. K. Sugimoto, *Characterization of Corrosion Products on Steel Surfaces*, ed. Y. Waseda and S. Suzuki (Springer, Heidelberg, Germany) p. 1 (2006).
57. Y. Waseda and S. Suzuki, *Characterization of Corrosion Products on Steel Surfaces* (Springer, Heidelberg, Germany) (2006).
58. T. Hanawa, S. Hiromoto, A. Yamamoto, D. Kuroda, and K. Asami, *Mater. Trans.*, **43**, 3088 (2002).
59. H. Yamaguchi, O. Fergani, and P.-Y. Wu, *CIRP Ann.*, **66**, 305 (2017).
60. N. Zhou, R. Pettersson, M. Schönning, and R. L. Peng, *Mater. Corros.*, **69**, 1560 (2018).
61. D. Kong, X. Ni, C. Dong, L. Zhang, C. Man, J. Yao, K. Xiao, and X. Li, *Electrochim. Acta*, **276**, 293 (2018).
62. S.-H. Sun, T. Ishimoto, K. Hagihara, Y. Tsutsumi, T. Hanawa, and T. Nakano, *Scr. Mater.*, **159**, 89 (2019).
63. Q. Chao, V. Cruz, S. Thomas, N. Birbilis, P. Collins, A. Taylor, P. D. Hodgson, and D. Fabijanic, *Scr. Mater.*, **141**, 94 (2017).
64. Y. Hedberg, O. Karlsson, P. Szakalos, and I. Odnevall Wallinder, *Mater. Lett.*, **65**, 2089 (2011).
65. I. E. Anderson and R. L. Terpstra, *Mater. Sci. Eng. A*, **326**, 101 (2002).
66. D. Riabov, E. Hryha, M. Rashidi, S. Bengtsson, and L. Nyborg, *Surf. Interf. Anal.*, .
67. J. Stewart and D. E. Williams, *Corros. Sci.*, **33**, 457 (1992).
68. C. Carboni, P. Peyre, G. Béranger, and C. Lemaitre, *J. Mater. Sci.*, **37**, 3715 (2002).
69. D. Kong, X. Ni, C. Dong, X. Lei, L. Zhang, C. Man, J. Yao, X. Cheng, and X. Li, *Mater. Design*, **152**, 88 (2018).
70. X. Ni, D. Kong, W. Wu, L. Zhang, C. Dong, B. He, L. Lu, K. Wu, and D. Zhu, *J. Mater. Eng. Perform.*, **27**, 3667 (2018).
71. J. A. Cherry, H. M. Davies, S. Mehmood, N. P. Lavery, S. G. R. Brown, and J. Sienz, *Int. J. Adv. Manuf. Tech.*, **76**, 869 (2015).